



Noncontrast Computed Tomography-Based Radiomics Analysis in Discriminating Early Hematoma Expansion after Spontaneous Intracerebral Hemorrhage

Zuhua Song, BS¹, Dajing Guo, MD, PhD¹, Zhuoyue Tang, MD, PhD², Huan Liu, MD³, Xin Li, BS¹, Sha Luo, BS¹, Xueying Yao, BS¹, Wenlong Song, BS¹, Junjie Song, BS¹, Zhiming Zhou, MS¹

¹Department of Radiology, The Second Affiliated Hospital of Chongqing Medical University, Chongqing, China; ²Department of Radiology, Chongqing General Hospital, Chongqing, China; ³GE Healthcare, Shanghai, China

Objective: To determine whether noncontrast computed tomography (NCCT) models based on multivariable, radiomics features, and machine learning (ML) algorithms could further improve the discrimination of early hematoma expansion (HE) in patients with spontaneous intracerebral hemorrhage (sICH).

Materials and Methods: We retrospectively reviewed 261 patients with sICH who underwent initial NCCT within 6 hours of ictus and follow-up CT within 24 hours after initial NCCT, between April 2011 and March 2019. The clinical characteristics, imaging signs and radiomics features extracted from the initial NCCT images were used to construct models to discriminate early HE. A clinical-radiologic model was constructed using a multivariate logistic regression (LR) analysis. Radiomics models, a radiomics-radiologic model, and a combined model were constructed in the training cohort (n = 182) and independently verified in the validation cohort (n = 79). Receiver operating characteristic analysis and the area under the curve (AUC) were used to evaluate the discriminative power.

Results: The AUC of the clinical-radiologic model for discriminating early HE was 0.766. The AUCs of the radiomics model for discriminating early HE built using the LR algorithm in the training and validation cohorts were 0.926 and 0.850, respectively. The AUCs of the radiomics-radiologic model in the training and validation cohorts were 0.946 and 0.867, respectively. The AUCs of the combined model in the training and validation cohorts were 0.960 and 0.867, respectively.

Conclusion: NCCT models based on multivariable, radiomics features and ML algorithm could improve the discrimination of early HE. The combined model was the best recommended model to identify sICH patients at risk of early HE.

Keywords: Hematoma expansion; Radiomics; Machine learning; Intracerebral hemorrhage; Computed tomography

INTRODUCTION

Intracerebral hemorrhage (ICH), accounts for 10–30% of all strokes, and is considered the most lethal type of stroke due to its high rate of disability and mortality (1, 2). It has been reported that the mortality rate of ICH ranges from 30% to 50% within 30 days after onset (3, 4).

Hematoma expansion (HE), which occurs in nearly 30% of ICH patients, is an independent prognostic and modifiable factor for mortality and poor outcomes in ICH patients (5-7). Therefore, it is of great significance to accurately discriminate patients at the highest risk for HE, as this could influence clinical management decisions.

As the first reported and widely accepted imaging sign,

Received: March 10, 2020 **Revised:** May 26, 2020 **Accepted:** July 2, 2020

This study was supported by the medical research Key Program of the combination of Chongqing National health commission and Chongqing science and technology bureau, China (no 2019ZDXM010); the Basic and Frontier Research Project of Chongqing, China (no cstc2016jcyjA0294).

Corresponding author: Zhiming Zhou, MS, Department of Radiology, The Second Affiliated Hospital of Chongqing Medical University, No. 74 Linjiang Rd, Yuzhong District, Chongqing 400010, China.

• E-mail: zhouzhiming1127@cqmu.edu.cn

This is an Open Access article distributed under the terms of the Creative Commons Attribution Non-Commercial License (<https://creativecommons.org/licenses/by-nc/4.0>) which permits unrestricted non-commercial use, distribution, and reproduction in any medium, provided the original work is properly cited.

the computed tomography angiography (CTA) spot sign is a reliable and effective predictor of HE (8). However, considering the limitations of contrast agents and the urgency of emergency treatment, noncontrast computed tomography (NCCT) is necessary and more convenient than CTA for ICH patients. Imaging signs based on NCCT, including the black hole sign (9), swirl sign (10), blend sign (11), hypodensity (12), irregular shape and density heterogeneity (13), have been recently proposed to discriminate early HE after spontaneous intracerebral hemorrhage (sICH). These imaging signs, which could reflect the heterogeneous density of the hematoma, have a high predictive specificity of 77.0–95.5% (9–12). However, the predictive sensitivity and accuracy of these imaging signs are relatively low, which means that predicting HE according to these imaging signs may lead to missed diagnoses and large errors in disease diagnoses, thus affecting decision-making in clinical management.

Radiomics is a newly developed method and a quantitative analysis that extracts large amounts of imaging features with high throughput from radiological images. The machine learning (ML) method can automatically optimize models from large datasets with multiple variables using algorithms. The combination of radiomics and ML algorithms could greatly improve the predictive ability of models and is widely used in cancer detection and phenotypic subtype classification of solid cancers (14–17). Recent studies have also applied radiomics or radiological variables based on NCCT images to predict HE after sICH, and all models in these studies achieved good predictive performances (18–20). However, few studies have focused on combining the advantages of different variables, including clinical characteristics, imaging signs, radiomics features of hematoma, and ML algorithms to further improve the discriminating ability of HE, especially its sensitivity.

In this study, we aimed to construct four types of models based on ML algorithms, multivariable, and radiomics features derived from the NCCT images of hematoma and compared the performances of different models to find the best recommended model to discriminate early HE in patients with sICH.

MATERIALS AND METHODS

Patient Population

This retrospective study was approved by the Institutional Ethics Committee of our hospital (decision number [2019]

19), and the need for written informed consent was waived.

In our hospital, 1016 patients with sICH were screened from our Picture Archiving and Communication Systems between April 2011 and March 2019. We included patients over 18 years old with sICH who underwent an initial CT examination within 6 hours of ictus and a follow-up CT examination within 24 hours after the initial CT. The exclusion criteria were as follows: patients who underwent surgical treatment before the follow-up CT; patients with secondary ICH, such as arteriovenous malformation, aneurysm, head trauma or brain tumor; patients with hemorrhagic evolution of an ischemic infarct; patients with primary intraventricular hemorrhage; patients with artifacts in their CT images; and patients with multifocal cerebral hemorrhage or a maximum length of the baseline hematoma less than 3 mm. Finally, 261 patients with sICH admitted in our hospital were retrospectively reviewed. The flow diagram of the patient selection process is displayed in Figure 1A.

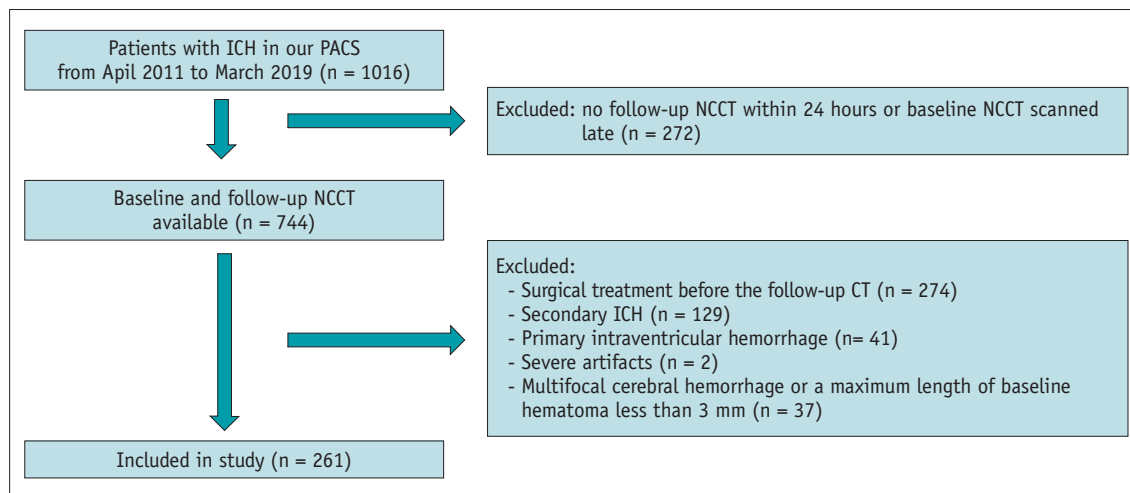
HE was defined as a proportional increase in hematoma volume > 33% or an absolute growth in the hematoma volume > 6 mL on the follow-up CT scan from the initial CT scan (6, 21). According to the definition of HE, all sICH patients were assigned into two groups: an expander group ($n = 110$) and a nonexpander group ($n = 151$).

The baseline demographic information, clinical characteristics and laboratory tests of the two groups, including sex, age, blood pressure at admission, important previous medical history (diabetes mellitus, hypertension), admission variables (Glasgow coma scale, time of symptom onset), and admission laboratory test results (apolipoprotein A-I [apoA-I], high-density lipoprotein cholesterol, low-density lipoprotein cholesterol, creatinine, urea, uric acid, activated partial thromboplastin time, international normalized ratio, fibrinogen level, and platelet count) were extracted from the electronic medical record system.

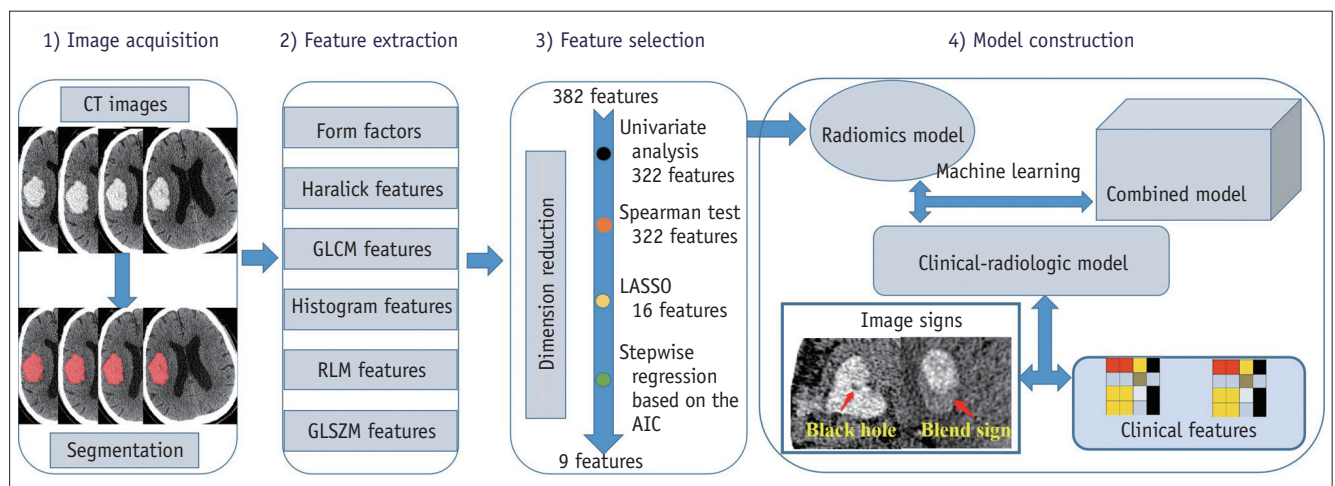
CT Examination and Image Analysis

CT images of 187 patients were obtained with a 128-slice CT scanner (Ingenuity, Philips Medical Systems) and those of 74 other patients were acquired with a 320-slice CT scanner (Aquilion ONE, Canon Medical Systems). The image acquisition parameters included a tube voltage of 120 kV, smart mAs, matrix size of 512 x 512, and slice thickness of 1 mm or 5 mm.

To reduce the discrepancies in the image acquisition parameters using two different CT scanners, we resampled all voxels into 1.0 x 1.0 x 1.0 mm³ from the raw data before



A



B

Fig. 1. System overview.

A. Flow diagram of the ICH patient selection process. **B.** The workflow of the radiomics analysis of hematoma. AIC = Akaike information criterion, GLCM = the gray-level cooccurrence matrix, GLSZM = the gray-level size zone matrix, ICH = intracerebral hemorrhage, LASSO = least absolute shrinkage and selection operator, NCCT = noncontrast computed tomography, PACS = Picture Archiving and Communication Systems, RLM = the run-length matrix

image analysis. To assess the consistency of the extracted radiomics features from different CT scanners, the intraclass correlation coefficient (ICC) of each feature in 20 sICH patients with HE scanned by using a 320-slice CT scanner and 20 age- and gender-matched patients scanned by using a 128-slice CT was calculated, and the study only continued if more than 90% of the features from initial CT images of two different scanners showed good consistency (ICC > 0.7).

NCCT imaging signs, including the black hole sign, swirl sign, blend sign, hypodensity, irregular shape and density heterogeneity, were assessed and recorded. The definitions of NCCT imaging signs are detailed in the Supplementary Materials. The procedure was performed independently by three radiologists who were blinded to the clinical

characteristics of patients to provide a final consensus.

Image Segmentation and Radiomics Feature Extraction

All the included patients were randomly split into a training cohort (n = 182) and a validation cohort (n = 79) according to a 7:3 ratio for model construction and validation. An in-house software (Artificial Intelligence Kit [AK] version 3.2.2, GE Healthcare) was used for CT image alignment. ITK-SNAP software (<http://www.itk-snap.org/pmwiki/pmwiki.php>) was used for three-dimensional whole-hematoma segmentation in the cohorts. The region of interest (ROI) was manually delineated around the boundary of the hematoma on each slice by a radiologist with 5 years of experience in neuroimaging.

To ensure the accuracy of the ROIs, 40 patients were randomly selected, and the ROIs were drawn again by another radiologist using the same method. The ICC of the ROIs in the 40 patients was calculated, and the study continued only if the ICC was > 0.7.

In total, 396 radiomics features were extracted automatically from each case using the AK software. The extracted radiomics features were classified as follows: histogram features, Haralick features, form factors, the gray-level cooccurrence matrix (GLCM), the run-length matrix (RLM), and the gray-level size zone matrix (GLSZM).

Radiomics Features Analysis

Dimension reduction was performed as described in Figure 1B. First, the ICC value for each feature was calculated to assess its reproducibility, and 382 of the 396 (96%) extracted radiomics features from the segmented hematoma regions of the initial CT images presented high stability (ICC > 0.7) and were entered into the following analysis. Second, univariate analysis was performed using the Mann-Whitney U test for continuous variables, and a *p* value < 0.05 was considered statistically significant. Third, Spearman correlation analysis was used to eliminate high-dimensional feature redundancy. After conducting the Mann-Whitney U test and Spearman correlation analysis, 322 significant features with *p* values < 0.05 were included in the following analysis. Last, the least absolute shrinkage and selection operator and stepwise

regression based on the Akaike information criterion were used to select the most powerful radiomics features. After the above steps, only 9 radiomics features were selected as the input of radiomics models (Fig. 2), including 3 RLM features (LongRunLowGrayLevelEmphasis_angle90_offset7, ShortRunHighGrayLevelEmphasis_AllDirection_offset7_SD, ShortRunEmphasis_angle45_offset1), 2 GLSZM features (HighIntensityLargeAreaEmphasis, LowIntensityLargeAreaEmphasis), 2 GLCM features (Correlation_angle90_offset4, HaralickCorrelation_AllDirection_offset1_SD), 1 form feature (SurfaceVolumeRatio), and 1 histogram feature (Quantile0.025). Spearman's correlation was performed to analyze the relationship between radiomics features and the degree of HE (absolute or relative sICH volume growth) in the expander group, and the results are shown in Supplementary Table 1.

Model Construction and Machine Learning

The clinical-radiologic model: univariate analysis was used to determine predictors among the clinical and radiological variables of all the included patients. The variables with *p* values < 0.05 were entered into the multivariate logistic regression (LR) analysis, and 4 clinical characteristics including sex, diabetes mellitus, platelet count, and apoA-I, and 4 imaging signs including the blend sign, black hole sign, swirl sign, and heterogeneity were used to construct the clinical-radiologic model.

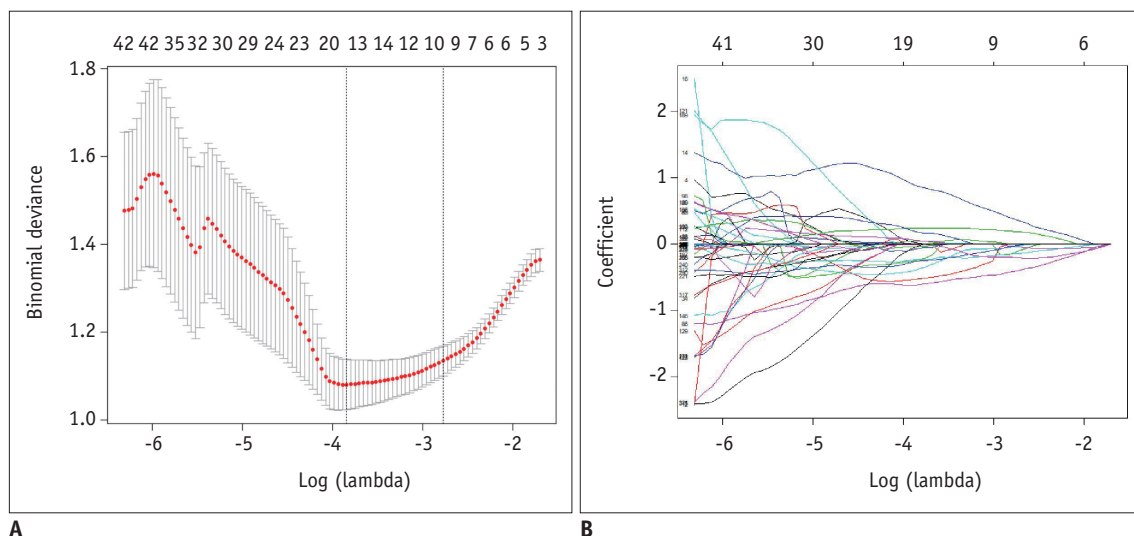


Fig. 2. Radiomics feature selection by means of the LASSO.

A. LASSO regression with 10-fold cross-validation was applied to select the radiomics features that could predict hematoma expansion. Tuning parameter selection in LASSO regression. **B.** LASSO coefficient analysis of the 322 radiomics features. Using 10-fold cross-validation, 16 non-zero coefficients were selected.

Radiomics models: nine radiomics features and 5 different ML algorithms were used to construct models in the training cohort. The ML algorithms included the naïve Bayes (NB), random forest (RF), LR, support vector machine (SVM), and k-nearest neighbors (KNN) algorithms. These models were independently verified in the validation cohort. The LR algorithm was the second best in the training cohort (the area under the curve [AUC] = 0.926) and in the validation cohort (AUC = 0.850), and was regarded as the suitable ML method for decreasing the influence of overfitting.

The radiomics-radiologic model: nine radiomics features, 4 imaging signs and the LR algorithm were used to construct the model in the training cohort, and the model was also independently verified in the validation cohort.

The combined model: nine radiomics features, 4 imaging signs, 4 clinical characteristics and the LR algorithm were used to construct the model in the training cohort, and the model was also independently verified in the validation cohort.

Model Evaluation

Receiver operating characteristic (ROC) curves for all models were generated, and AUC, specificity and sensitivity were calculated to evaluate the discriminative ability of each model. The DeLong test was used to compare the discriminative performance of different models. Decision curve analysis (DCA) was conducted to assess the clinical usefulness of different radiomics models.

Statistical Analysis

Statistical analysis was performed using the R software (version 3.6.0; <http://www.Rproject.org>). Continuous variables were expressed as medians (interquartile ranges), and categorical variables as frequencies (percentages). The Shapiro-Wilk test was applied to check the normality of continuous variables. The Mann-Whitney U test was used for non-normally distributed data. Two-sample *t* tests were used for normally distributed data. Chi-square test or Fisher's exact test were applied to compare categorical variables. A two-tailed $p < 0.05$ was considered statistically significant.

RESULTS

The demographic data, clinical characteristics, laboratory tests and imaging signs of the expander group and nonexpander group are given in Table 1. Only sex, diabetes

mellitus, platelet count, apoA-I and the 5 imaging signs (blend sign, black hole sign, swirl sign, hypodensity [type 1] and hypodensity [type 3], heterogeneity) were significantly different between the two groups (Table 1).

The ROC curves of the 5 imaging signs are shown in Figure 3A. Among the 5 imaging signs, the black hole sign had the highest AUC for discriminating HE after sICH (AUC = 0.610), and its specificity and sensitivity were 0.853 and 0.367, respectively. The ROC curves of the clinical-radiologic model are shown in Figure 3B. The AUC, specificity and sensitivity of this model were 0.766, 0.775, and 0.645, respectively.

Performance of the Radiomics Models and Verification

The ROC curves of the five radiomics models in the training cohort and in the validation cohort are shown in Figure 4A and B. The DeLong test showed that the AUCs of the radiomics models were significantly higher than those of the clinical-radiologic model in discriminating HE (p values were 0.001, 0.003, 0.001, 0.002, and 0.003 for LR, NB, RF, SVM, and KNN, respectively), with no significant difference between the AUC of the radiomics model built using the LR algorithm and that built using the 4 other algorithms in the validation cohort (p values were 0.052, 0.710, 0.590, and 0.300 for NB, RF, SVM, and KNN, respectively). The AUCs, specificities and sensitivities of the radiomics model built using the LR algorithm were 0.926, 0.914, and 0.818 in the training cohort, and 0.850, 0.818, and 0.761 in the validation cohort, respectively. The decision curves of the five radiomics models showed that all models for predicting early HE were better than the treat-all-patients measures and the treat-none measures (Fig. 4C, D).

The radiomics-radiologic model showed a better performance than the clinical-radiologic model, with an AUC of 0.946, specificity of 0.943 and sensitivity of 0.805 in the training cohort ($p = 0.001$, DeLong test), and AUC of 0.867, specificity of 0.879 and sensitivity of 0.795 in the validation cohort ($p = 0.001$, DeLong test), (Fig. 5A, B).

The combined model showed a satisfactory performance similar to the radiomics-radiologic model, with an AUC of 0.960, specificity of 0.952 and sensitivity of 0.844 in the training cohort, and an AUC of 0.867, specificity of 0.881 and sensitivity of 0.804 in the validation cohort (Fig. 5C, D).

DISCUSSION

In this retrospective study, we constructed four types of models including the clinical-radiologic model, radiomics

Table 1. Patient Characteristics

Variables	Expanders (n = 110)	Nonexpanders (n = 151)	P
Male, sex	75 (68.1)	84 (55.6)	0.040*
Age, year	62 (51–71)	61 (51–69)	0.473
Onset-to-CT time, hour	2.0 (1.5–3.0)	3.0 (2.0–4.0)	0.393
Admission SBP, mm Hg	176 (159–196)	176 (155–195)	0.623
Admission DBP, mm Hg	100 (84–110)	100 (90–112)	0.212
Diabetes mellitus	42 (38.1)	38 (25.1)	0.021*
Hypertension	65 (59.1)	95 (62.9)	0.533
Platelets, x 10 ⁹ /L	160.5 (121.8–201.8)	184.0 (148.0–227.0)	0.013*
APTT, second	33.6 (31.3–37.0)	34.4 (31.6–38.1)	0.329
INR	1.02 (0.95–1.08)	1.03 (0.98–1.08)	0.987
Fibrinogen, g/L	2.93 (2.63–3.53)	3.03 (2.56–3.44)	0.587
Creatinine, μmol/L	61.65 (46.15–82.03)	60.2 (47.70–73.0)	0.465
Urea, mmol/L	5.73 (4.62–7.03)	5.36 (4.34–6.50)	0.908
Uric acid, μmol/L	284.7 (207.1–347.2)	293.0 (227.6–385.3)	0.225
HDL-C, mmol/L	1.20 (1.00–1.44)	1.24 (1.05–1.48)	0.327
LDL-C, mmol/L	2.31 (1.74–3.01)	2.54 (1.99–2.91)	0.143
ApoA-I, g/L	1.50 (1.29–1.75)	1.56 (1.38–1.82)	0.024*
GCS score	12 (10–14)	13 (10–14)	0.114
Bleeding location	-	-	0.394
Deep	86 (32.9)	122 (46.7)	
Lobar	3 (1.1)	7 (2.7)	
Brain stem	16 (6.1)	18 (6.9)	
Cerebellum	5 (1.9)	4 (1.5)	
Initial sICH volume, mL	12.65 (6.59–24.22)	11.09 (5.52–20.08)	0.100
Absolute sICH volume growth, mL	10.55 (7.02–20.98)	0 (0–0.12)	< 0.001*
Relative sICH volume growth, %	92.5 (55.2–164.6)	0 (0–2.0)	< 0.001*
Blend sign	30 (27.3)	23 (15.2)	0.017*
Black hole sign	40 (36.4)	22 (14.6)	< 0.001*
Swirl sign	20 (20.0)	6 (4.0)	< 0.001*
SAH	8 (7.3)	10 (6.6)	0.838
Irregular shape	79 (71.2)	96 (63.5)	0.163
Hypodensity	-	-	-
Type 1	36 (32.7)	28 (18.5)	0.008*
Type 2	8 (7.3)	12 (7.9)	0.841
Type 3	6 (5.5)	0	0.003*
Type 4	1 (0.9)	0	0.242
Heterogeneity	46 (41.8)	40 (26.5)	0.009*

Data are noted as median and interquartile ranges or numbers and percentages in parenthesis. * $p < 0.05$. ApoA-I = apolipoprotein A-I, APTT = activated partial thromboplastin time, CT = computed tomography, DBP = diastolic blood pressure, GCS = Glasgow coma scale, HDL-C = high-density lipoprotein cholesterol, INR = international normalized ratio, LDL-C = low-density lipoprotein cholesterol, SAH = subarachnoid hemorrhage, SBP = systolic blood pressure, sICH = spontaneous intracerebral hemorrhage

model, radiomics-radiologic model, and combined model to discriminate early HE after sICH. Among these models, the combined model showed a satisfactory performance in the training cohort (AUC = 0.960) and validation cohort (AUC = 0.867) to discriminate HE, and can be used to effectively identify sICH patients at risk of early HE.

In this study, the clinical-radiologic model had a better

discriminative performance and a higher sensitivity (AUC = 0.766, sensitivity = 0.645) than the black hole sign (AUC = 0.610, sensitivity = 0.367). In the clinical-radiologic model, sex, apoA-I, diabetes mellitus, and the platelet count were independently associated with HE. Similar to our study, a previous study showed that men with ICH experience a higher risk of HE than women with ICH (22). Lower platelet

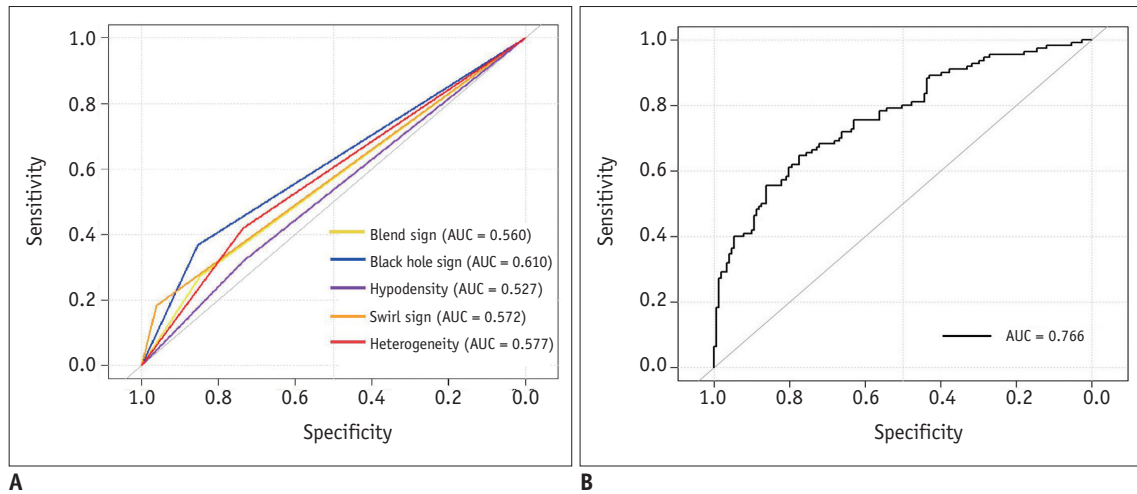


Fig. 3. ROC curves of the imaging signs and the clinical-radiologic model for predicting hematoma expansion.

A, B. The ROC curves of the five imaging signs and the clinical-radiologic model. AUC = the area under the curve, ROC = receiver operating characteristic

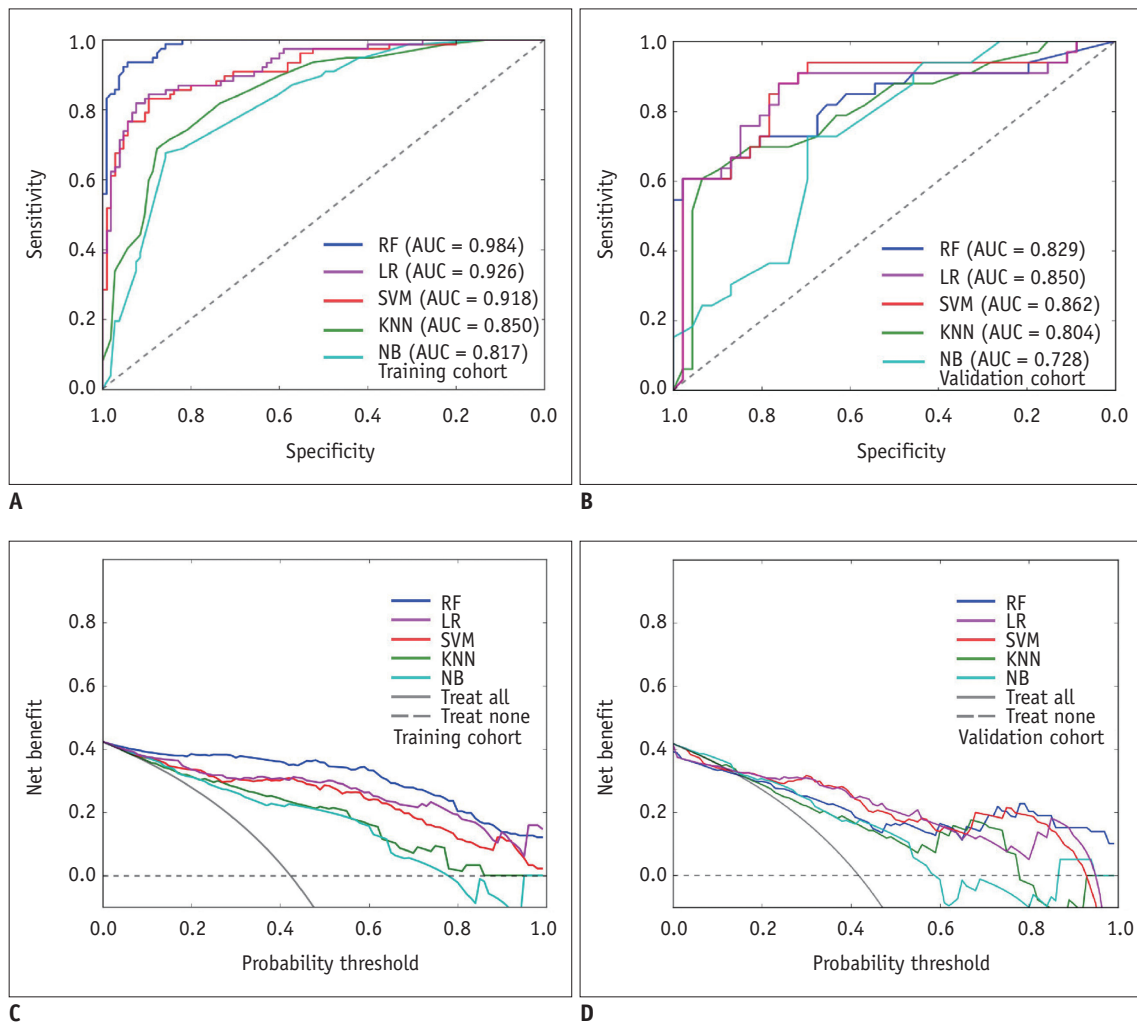


Fig. 4. ROC curves and decision curves of the five radiomics models for predicting hematoma expansion.

A, B. The ROC curves of the five radiomics models in the training cohort and in the validation cohort. **C, D.** The decision curves of the five radiomics models in the training cohort and in the validation cohort. KNN = k-nearest neighbors, LR = logistic regression, NB = naive Bayes, RF = random forest, SVM = support vector machine

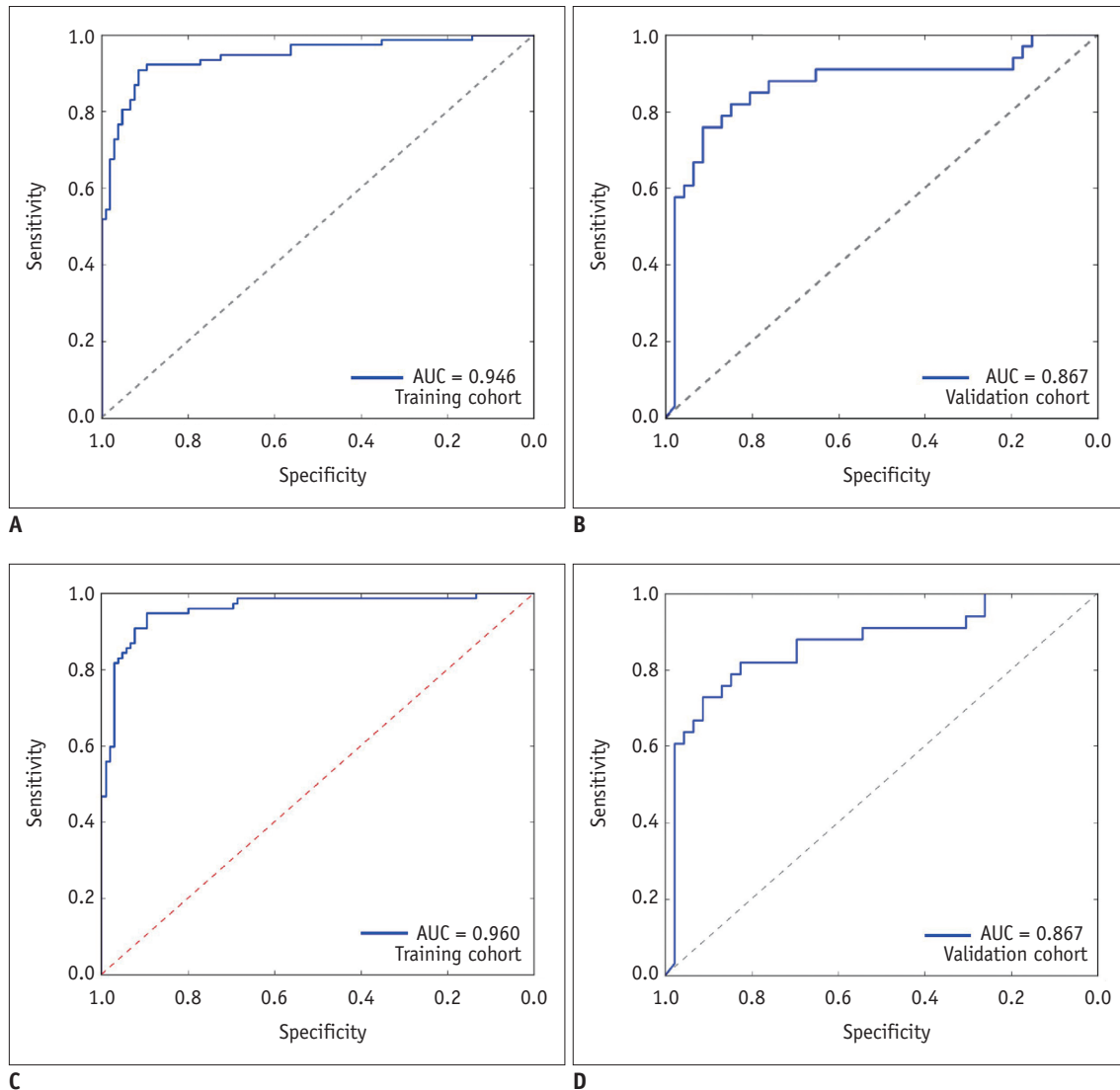


Fig. 5. ROC curves of the radiomics-radiologic model and the combined model for predicting hematoma expansion.
A, B. The ROC curves of the radiomics-radiologic model in the training cohort and the validation cohort. **C, D.** The ROC curves of the combined model in the training cohort and the validation cohort.

count can easily cause bleeding, which may be related to HE. The reduction in apoA-I may be associated with rupturing blood vessels, which could lead to HE (23). In addition, elevated serum glucose levels in diabetic patients could accelerate the destruction of the blood-brain barrier and impair the integrity of small cerebral vessels, which is likely to cause HE (24, 25). Consequently, by adding clinical characteristics, the discrimination capability and sensitivity of this model can be effectively improved.

In our study, the radiomics models demonstrated a better discrimination capability and higher sensitivity than the clinical-radiologic model. As reported, heterogeneity reflects different ongoing phases of bleeding and thus higher heterogeneity of the hematoma tends to mean a higher

risk of HE (12). Compared with imaging signs, radiomics features may have the advantages of a higher resolution and quantitative evaluation. A previous study suggested that NCCT texture analysis can objectively quantify the heterogeneity of ICH and independently predict early hematoma enlargement (19). In our study, 9 radiomics features belonging to the RLM, GLSZM, GLCM and histogram features that described the heterogeneity and shapes of the hematoma may be associated with active bleeding and HE after sICH.

Furthermore, ML algorithms can handle large numbers of imaging features and yield a potential predictive increase in accuracy over regression models (26, 27). In our study, we applied five common ML algorithms to construct radiomics

models to discriminate early HE after sICH, and all radiomics models showed good discrimination capabilities. More importantly, the LR algorithm was regarded as the suitable ML method for decreasing the influence of overfitting. However, this result was different from the best algorithm in Li et al.'s study (28). We speculate that different radiomics features, patients and parameters of the constructed model may be suitable for different ML algorithms, and the LR algorithm, which was especially suitable for constructing models with continuous and categorical independent variables, was more suitable for our data. Additionally, we used DCA to confirm that the radiomics model based on the LR algorithm could be widely used in clinical practice to discriminate patients at risk of HE. Nevertheless, it is necessary to standardize the radiomics features and samples to evaluate the optimal algorithm for discriminating HE in future research.

To further prove that models based on multivariable, radiomics features and ML algorithm can improve the discrimination of HE, we used the suitable LR algorithm to construct two other models (a radiomics-radiologic model and a combined model) to discriminate early HE after sICH. As expected, both models showed a good discrimination capability and sensitivity in detecting early HE after sICH. In line with our study, a combined model integrating radiological variables and a radiomics score showed a higher AUC than the radiomics model in predicting early HE in ICH patients (20). Thus, the better model for discriminating HE was based on many variables rather than a single variable. In addition, although the radiomics-radiologic model achieved a satisfactory discrimination capability in our results, the addition of 4 clinical characteristics can still improve the sensitivity of the combined model (sensitivity = 0.844) in the training cohort and (sensitivity = 0.804) in the validation cohort. According to the above results, to more sensitively and effectively discriminate early HE after sICH, our best recommended model was the combined model.

There are several limitations in this study. First, our study was a single-center retrospective study based on a small sample size, so our findings may not be generalizable to other centers. A larger prospective multicenter study in the future is needed to verify our findings. Second, only the features of hematoma were included in the models, which may limit the use of our recommended model. We did not analyze the correlation of perihematomal edema with HE, which may contribute to the discrimination of HE. Finally,

as mentioned above, standardized NCCT scans, feature extraction and selection, model construction and analysis are needed in the future.

In summary, we can improve the ability to detect early HE after sICH by constructing NCCT models based on multivariables, radiomics features, and ML algorithms. Among the four types of models constructed, the combined model was the best recommended model for discriminating the risk of early HE after sICH.

Supplementary Materials

The Data Supplement is available with this article at <https://doi.org/10.3348/kjr.2020.0254>.

Conflicts of Interest

The authors have no potential conflicts of interest to disclose.

ORCID iDs

Zuhua Song

<https://orcid.org/0000-0002-5752-4505>

Dajing Guo

<https://orcid.org/0000-0001-8655-6621>

Zhuoyue Tang

<https://orcid.org/0000-0002-1433-5966>

Huan Liu

<https://orcid.org/0000-0002-6700-962X>

Xin Li

<https://orcid.org/0000-0001-7154-3828>

Sha Luo

<https://orcid.org/0000-0002-0507-0273>

Xueying Yao

<https://orcid.org/0000-0001-5411-5346>

Wenlong Song

<https://orcid.org/0000-0001-7810-8466>

Junjie Song

<https://orcid.org/0000-0002-3982-7115>

Zhiming Zhou

<https://orcid.org/0000-0002-7028-7866>

REFERENCES

1. Ziai WC, Carhuapoma JR. Intracerebral hemorrhage. *Continuum (Minneapolis Minn)* 2018;24:1603-1622
2. Brouwers HB, Chang Y, Falcone GJ, Cai X, Ayres AM, Battey TW, et al. Predicting hematoma expansion after primary

- intracerebral hemorrhage. *JAMA Neurol* 2014;71:158-164
3. Poon MT, Fonville AF, Al-Shahi Salman R. Long-term prognosis after intracerebral haemorrhage: systematic review and meta-analysis. *J Neurol Neurosurg Psychiatry* 2014;85:660-667
 4. Hansen BM, Nilsson OG, Anderson H, Norrving B, Säveland H, Lindgren A. Long term (13 years) prognosis after primary intracerebral haemorrhage: a prospective population based study of long term mortality, prognostic factors and causes of death. *J Neurol Neurosurg Psychiatry* 2013;84:1150-1155
 5. Brouwers HB, Greenberg SM. Hematoma expansion following acute intracerebral hemorrhage. *Cerebrovasc Dis* 2013;35:195-201
 6. Dowlatshahi D, Demchuk AM, Flaherty ML, Ali M, Lyden PL, Smith EE, et al. Defining hematoma expansion in intracerebral hemorrhage: relationship with patient outcomes. *Neurology* 2011;76:1238-1244
 7. Davis SM, Broderick J, Hennerici M, Brun NC, Diringer MN, Mayer SA, et al. Hematoma growth is a determinant of mortality and poor outcome after intracerebral hemorrhage. *Neurology* 2006;66:1175-1181
 8. Wada R, Aviv RI, Fox AJ, Sahlas DJ, Gladstone DJ, Tomlinson G, et al. CT angiography "spot sign" predicts hematoma expansion in acute intracerebral hemorrhage. *Stroke* 2007;38:1257-1262
 9. Li Q, Zhang G, Xiong X, Wang XC, Yang WS, Li KW, et al. Black hole sign: novel imaging marker that predicts hematoma growth in patients with intracerebral hemorrhage. *Stroke* 2016;47:1777-1781
 10. Yu Z, Zheng J, He M, Guo R, Ma L, You C, et al. Accuracy of swirl sign for predicting hematoma enlargement in intracerebral hemorrhage: a meta-analysis. *J Neurol Sci* 2019;399:155-160
 11. Li Q, Zhang G, Huang YJ, Dong MX, Lv FJ, Wei X, et al. Blend sign on computed tomography: novel and reliable predictor for early hematoma growth in patients with intracerebral hemorrhage. *Stroke* 2015;46:2119-2123
 12. Boulouis G, Morotti A, Brouwers HB, Charidimou A, Jessel MJ, Auriel E, et al. Association between hypodensities detected by computed tomography and hematoma expansion in patients with intracerebral hemorrhage. *JAMA Neurol* 2016;73:961-968
 13. Barras CD, Tress BM, Christensen S, MacGregor L, Collins M, Desmond PM, et al. Density and shape as CT predictors of intracerebral hemorrhage growth. *Stroke* 2009;40:1325-1331
 14. Kumar V, Gu Y, Basu S, Berglund A, Eschrich SA, Schabath MB, et al. Radiomics: the process and the challenges. *Magn Reson Imaging* 2012;30:1234-1248
 15. Lambin P, Rios-Velazquez E, Leijenaar R, Carvalho S, van Stiphout RG, Granton P, et al. Radiomics: extracting more information from medical images using advanced feature analysis. *Eur J Cancer* 2012;48:441-446
 16. Tian Q, Yan LF, Zhang X, Zhang X, Hu YC, Han Y, et al. Radiomics strategy for glioma grading using texture features from multiparametric MRI. *J Magn Reson Imaging* 2018;48:1518-1528
 17. Ginsburg SB, Algohary A, Pahwa S, Gulani V, Ponsky L, Aronen HJ, et al. Radiomic features for prostate cancer detection on MRI differ between the transition and peripheral zones: preliminary findings from a multi-institutional study. *J Magn Reson Imaging* 2017;46:184-193
 18. Ma C, Zhang Y, Niyazi T, Wei J, Guocai G, Liu J, et al. Radiomics for predicting hematoma expansion in patients with hypertensive intraparenchymal hematomas. *Eur J Radiol* 2019;115:10-15
 19. Shen Q, Shan Y, Hu Z, Chen W, Yang B, Han J, et al. Quantitative parameters of CT texture analysis as potential markers for early prediction of spontaneous intracranial hemorrhage enlargement. *Eur Radiol* 2018;28:4389-4396
 20. Xie H, Ma S, Wang X, Zhang X. Noncontrast computer tomography-based radiomics model for predicting intracerebral hemorrhage expansion: preliminary findings and comparison with conventional radiological model. *Eur Radiol* 2020;30:87-98
 21. Demchuk AM, Dowlatshahi D, Rodriguez-Luna D, Molina CA, Blas YS, Dzialowski I, et al. Prediction of haematoma growth and outcome in patients with intracerebral haemorrhage using the CT-angiography spot sign (PREDICT): a prospective observational study. *Lancet Neurol* 2012;11:307-314
 22. Marini S, Morotti A, Ayres AM, Crawford K, Kourkoulis CE, Lena UK, et al. Sex differences in intracerebral hemorrhage expansion and mortality. *J Neurol Sci* 2017;379:112-116
 23. Jurukovska-Nospal M, Arsova V, Levchanska J, Sidovska-Ivanovska B. Effects of statins (atorvastatin) on serum lipoprotein levels in patients with primary hyperlipidemia and coronary heart disease. *Prilozi* 2007;28:137-148
 24. Zhang F, Zhang S, Tao C, Yang Z, Li X, You C, et al. Association between serum glucose level and spot sign in intracerebral hemorrhage. *Medicine (Baltimore)* 2019;98:e14748
 25. Allen CL, Bayraktutan U. Antioxidants attenuate hyperglycaemia-mediated brain endothelial cell dysfunction and blood-brain barrier hyperpermeability. *Diabetes Obes Metab* 2009;11:480-490
 26. Asadi H, Dowling R, Yan B, Mitchell P. Machine learning for outcome prediction of acute ischemic stroke post intra-arterial therapy. *PLoS One* 2014;9:e88225
 27. Singal AG, Mukherjee A, Elmunzer BJ, Higgins PD, Lok AS, Zhu J, et al. Machine learning algorithms outperform conventional regression models in predicting development of hepatocellular carcinoma. *Am J Gastroenterol* 2013;108:1723-1730
 28. Li H, Xie Y, Wang X, Chen F, Sun J, Jiang X. Radiomics features on non-contrast computed tomography predict early enlargement of spontaneous intracerebral hemorrhage. *Clin Neurol Neurosurg* 2019;185:105491